2D MATERIALS

Crossover between strongly coupled and weakly coupled exciton superfluids

Xiaomeng Liu[1]†, J. I. A. Li[2]†, Kenji Watanabe[3], Takashi Taniguchi[4], James Hone[5], Bertrand I. Halperin[1], Philip Kim[1]*, Cory R. Dean[6]*

In fermionic systems, superconductivity and superfluidity occur through the condensation of fermion pairs. The nature of this condensate can be tuned by varying the pairing strength, which is challenging in electronic systems. We studied graphene double layers separated by an atomically thin insulator. Under applied magnetic field, electrons and holes couple across the barrier to form bound magneto-excitons whose pairing strength can be continuously tuned by varying the effective layer separation. Using temperature-dependent Coulomb drag and counterflow current measurements, we were able to tune the magneto-exciton condensate through the entire phase diagram from weak to strong coupling. Our results establish magneto-exciton condensates in graphene as a model platform to study the crossover between two bosonic quantum condensate phases in a solid-state system.

In the presence of attractive interactions, a fermionic system can become unstable against pairing, forming composite bosons. These paired fermions then can form a low-temperature condensate phase. It has long been recognized that the nature of the fermionic condensate and its phase transition are directly governed by the strength of the pairing interaction U relative to the Fermi energy E_F (Fig. 1A) (*1*–*4*). Electrons in metals provide a paradigm example of the weak-coupling regime, where the pairing interaction is small relative to the Fermi energy ($U << E_F$). A low-temperature superconducting phase emerges from this weakly interacting Fermi liquid, described by the Bardeen-Cooper-Schrieffer (BCS) theory (*5*). In this regime, electrons near the Fermi surface form pairs in momentum space, with the size of the resulting Cooper pair usually much larger than interparticle distance (*2*). In the opposite limit of strong interactions ($U >> E_F$), fermions form spatially tightly bound pairs, and the size of the pair is much smaller than the average interparticle separation. In this strongly coupled limit, the system behaves like a bosonic gas or liquid, instead of like a Fermi liquid, and the low-temperature ground state is characterized by a Bose-Einstein condensate (BEC).

A crossover between the BEC and BCS regimes can theoretically be realized by tuning the ratio of U/E_F (*6*–*8*), which also corresponds to tuning the ratio of the "size" of the fermion pairs versus the interbosonic particle spacing. In solid-state systems, where the most prominent fermionic condensates (i.e., superconductors) are found, the BEC-BCS crossover paradigm is highly relevant: Whereas most metallic superconductors are understood to be in the BCS limit, some unconventional superconductors, such as the high-T_c cuprates (*3*, *9*–*11*), and twisted bilayer graphene (*12*) are thought to reside near the crossover ($U \sim E_F$) between the BEC and BCS limits. In cold-fermion gases, continuous tuning between the weak-coupling and strong-coupling limits has been demonstrated, and the unitary crossover regime has been firmly established (*13*–*18*). Demonstration of this same crossover in a solid-state platform (i.e., within a single electronic superconductor) has been realized only recently because of the difficulty of continuously tuning the coupling strength (e.g., varying U at fixed E_F) or the electron density (varying E_F at fixed U) sufficiently while maintaining the condensate ground state (*19*–*22*).

We examined the crossover behavior of the condensate phase of magneto-excitons in quantum Hall bilayer (QHB) systems. Superfluidic magneto-exciton condensation was first realized in QHBs fabricated from GaAs heterostructures (*23*) and later from graphene double layers (*24*, *25*). Here, electron-like and hole-like quasi-particles of partially filled Landau levels (LLs) reside in two parallel conducting layers. At integer values of the combined LL filling fraction $\nu_{tot} = \nu_{top} + \nu_{bot}$, where ν_{top} and ν_{bot} are respectively the filling fractions of the top and bottom layers, electrons in one layer and holes in the other layer can pair up, forming interlayer excitons that then condense into a superfluid state at low temperatures (*23*).

Unlike in metallic superconductors, the pairing between fermions in QHB systems is widely tunable. Because the kinetic energy of electrons is quenched in the LLs, the energetics of this system is determined by the competition between the intralayer Coulomb interaction $E_c = e^2/\varepsilon l_B$ (in Gaussian units), where $l_B = \sqrt{\hbar/eB}$ is the magnetic length, ε is the background dielectric constant, $\hbar$ is the reduced Planck constant, e is electron charge, and B is magnetic field, and the attractive interlayer Coulomb interaction between an isolated electron and hole in the lowest LL, $U \approx (e^2/\varepsilon)/(d + 0.8l_B)$, where d is the interlayer separation (Fig. 1B) (*26*). For an isolated layer with a partially filled LL, a Chern-Simons gauge transformation can turn its strongly interacting electrons characterized by E_c to a composite Fermi liquid with Fermi energy $E_F \propto E_c$ (*27*). In QHBs, the ratio U/E_c, which is solely determined by d/l_B, therefore provides a characterization of the relative pairing strength, analogous to the dimensionless parameter U/E_F for generic fermionic systems with dispersive bands (*23*, *28*, *29*). For $d << l_B$, U is on the order of E_F, resulting in relatively tightly bound electron-hole pairs, which persist at temperatures well above the transition temperature where the Bose condensate disappears. For $d >> l_B$, the two layers are only weakly coupled, with each layer described by a composite Fermi liquid. In this limit, interaction between the two Fermi surfaces can lead to a pairing instability at low temperatures, resulting in a BCS-like condensate (*26*, *30*–*34*).

Experimentally, d/l_B can be continuously varied in a single device, by varying the applied magnetic field B, or across multiple devices, by changing the interlayer distance d. This provides the opportunity to continuously tune through the complete condensate phase diagram. In our study, we fabricated QHBs from graphene double layers consisting of two parallel graphene layers separated by a dielectric tunneling barrier consisting of a few layers of hexagonal boron nitride (hBN) (Fig. 1B and fig. S1). We focus on the magneto-exciton condensate appearing at $\nu_{tot} = -1$, corresponding to both layers filled to half filling of the first hole LL ($\nu_{top} = \nu_{bot} = -½$). We report results over the range $0.3 < d/l_B < 0.8$, where well-defined exciton superfluid states exist at the lowest experimental temperature.

To probe the dynamics of the interlayer exciton, we used the Coulomb drag and counterflow geometries (*35*–*38*) (Fig. 1D, inset) (*26*). In the Coulomb drag geometry, the exciton condensate is identified by the emergence of a quantized Hall resistance plateau equal to h/e^2, as measured in both the drive and drag layers, concomitant with zero longitudinal resistance in both layers (Fig. 1D). In contrast, when the two layers are decoupled, the drive layer exhibits a density-dependent Hall resistance, whereas the Hall resistance of the drag layer is close to zero (*39*). Thus, the Hall drag resistance R_{xy}^{drag} provides an experimental measure of interlayer pairing (*23*–*25*). In the

[1]Department of Physics, Harvard University, Cambridge, MA 02138, USA. [2]Department of Physics, Brown University, Providence, RI 02912, USA. [3]Research Center for Functional Materials, National Institute for Materials Science, 1-1 Namiki, Tsukuba 305-0044, Japan. [4]International Center for Materials Nanoarchitectonics, National Institute for Materials Science, 1-1 Namiki, Tsukuba 305-0044, Japan. [5]Department of Mechanical Engineering, Columbia University, New York, NY 10027, USA. [6]Department of Physics, Columbia University, New York, NY 10027, USA.
*Corresponding author. Email: pkim@physics.harvard.edu (P.K.); cd2478@columbia.edu (C.R.D.)
†These authors contributed equally to this work.

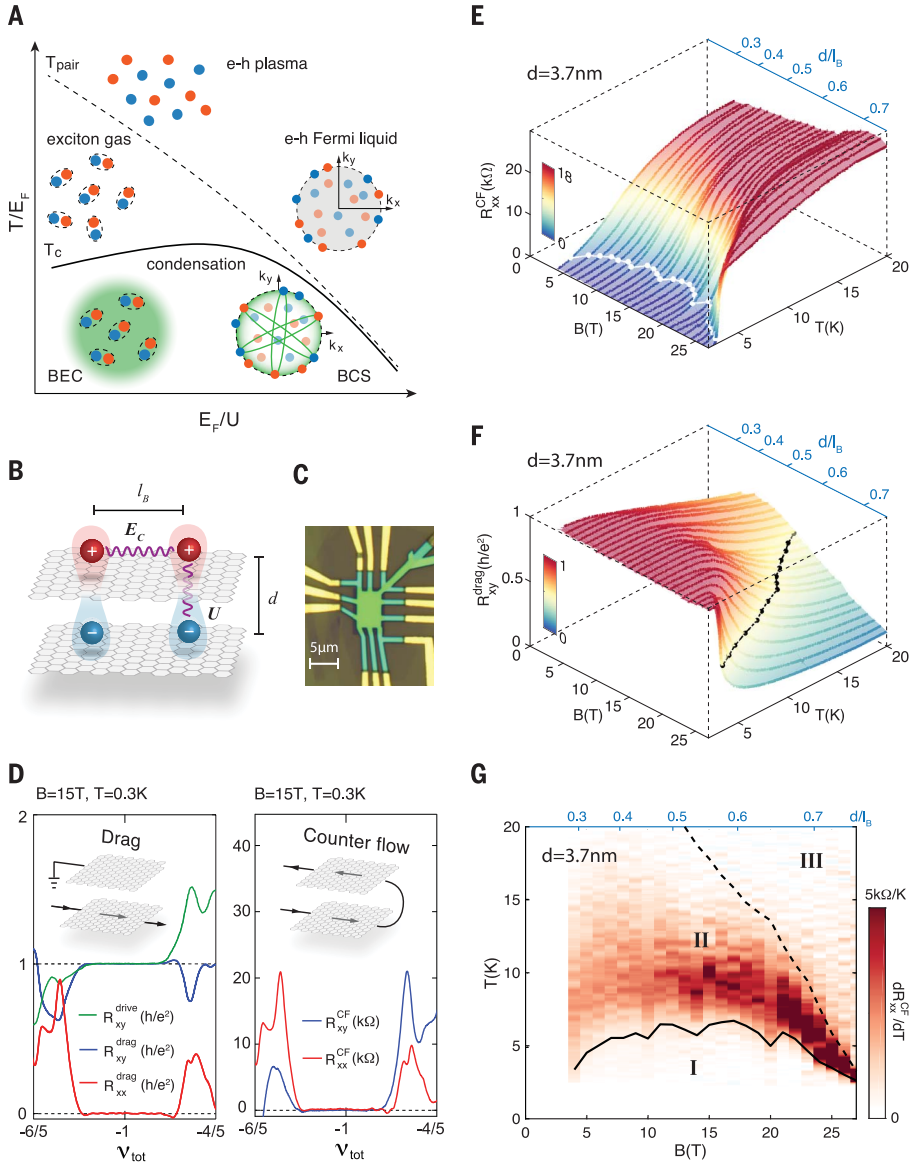

Fig. 1. Two regimes of the exciton condensate. (**A**) Schematic phase diagram for equal densities of electrons and holes with varying temperature and coupling strength. The temperature axis is in units of the Fermi energy E_F. In the strong coupling limit ($E_F/U << 1$), the electrons (orange circles) and holes (blue circles) start to pair at T_{pair} and condense at much lower temperature T_c. The green halo signifies the condensate. In the weak coupling limit ($E_F/U >> 1$), the electrons and holes exist as Fermi liquids at high temperatures and establish the BCS type of pairing below T_c. Wave vectors k_x and k_y are indicated; the green lines denote pairing between electrons and holes on the Fermi surface. (**B**) Illustration of the energy and length scales associated with exciton pairing in a graphene double-layer structure under a magnetic field. Interlayer Coulomb coupling U depends on the interlayer separation d, whereas intralayer Coulomb repulsion E_c is determined by the magnetic length l_B. (**C**) Optical image of a graphene double-layer device used in this study. (**D**) Left: Coulomb drag response of exciton condensate at $\nu_{tot} = -1$. Inset: Schematic for the drag measurement setup; arrow indicates the direction of current flow in the drive layer. Right: Longitudinal and Hall resistance in counterflow geometry measured at $\nu_{tot} = -1$. Inset: Schematic for counterflow measurement setup. Arrows indicate the direction of current flow in each layer. (**E**) Waterfall plot of longitudinal resistance from counterflow measurement as a function of temperature measured for a range of B values. The white line marks the superfluid transition temperature, T_c, where R_{xx}^{CF} drops to near zero. (**F**) Waterfall plot of Hall drag response as a function of temperature measured for a range of B values. The black dashed line marks the pairing temperature, T_{pair}, where the Hall drag is half of the quantized value. (**G**) Temperature derivative of R_{xx}^{CF} as a function of temperature T and magnetic field B. The black solid and dashed lines mark T_c and T_{pair}, respectively, according to their definitions in (E) and (F). The corresponding d/l_B value is marked on the top axis. Area I corresponds to a condensate, area II to the normal states of excitons, and area III to the normal states of disassociated electrons and holes.

counterflow geometry, charge-neutral excitons can be induced to flow by configuring the current to move in opposite directions in the two layers (*40*). In this geometry, the neutral exciton current gives a zero-valued Hall resistance in both layers, and the dissipationless nature of the superfluid condensate is revealed by a vanishing longitudinal resistance (Fig. 1D).

Figure 1, E and F, shows the temperature dependence of the counterflow longitudinal resistance R_{xx}^{CF} and the Hall drag resistance R_{xy}^{drag} of a d = 3.7 nm device, for a range of values of d/l_B obtained by varying the magnetic field B (see also fig. S2). At low temperatures, the exciton superfluid phase was observed over the full range of effective layer separation that we studied, $0.3 < d/l_B < 0.8$, as evidenced by the vanishing R_{xx}^{CF} in counterflow and quantized R_{xy}^{drag} (*23*, *36*–*38*).

The temperature evolution of these quantities across different values of d/l_B allowed us to experimentally map key features of the condensate phase diagram. First, we identified the critical temperature of the condensate as the value below which the longitudinal transport becomes dissipationless. We defined this point as the temperature where R_{xx}^{CF} drops to less than 5% of the high-temperature saturation value. Indicated by a white line in Fig. 1E, this boundary identifies a dome below which the condensate is well formed. The dome shape of the critical temperature is consistent with theoretical expectation (*29*). In the strong coupling limit (small d/l_B), the primary consequence of increasing B is a corresponding increase of the exciton density ($\propto B$), which in turn drives up T_c. Conversely, in the weak coupling limit (large d/l_B), increasing d/l_B further reduces the interlayer coupling, resulting in a diminishing of the pairing between the two Fermi liquids and causing T_c to decrease.

Second, we interpret R_{xy}^{drag} as a measure of the pair fraction. In the limit of strong coupling, where electrons and holes occur in tightly bound pairs, excitons may persist at temperatures well above the counterflow-superconductivity critical temperature. In this temperature range, we would still expect to observe a large R_{xy}^{drag} response. On the other hand, at temperatures sufficiently high that electrons and holes are dissociated, the value of R_{xy}^{drag} will be close to zero. We can therefore identify a temperature scale for the pair-breaking by the temperature where R_{xy}^{drag} deviates from the quantized value h/e^2. Phenomenologically, we define the pair-breaking temperature T_{pair} as the temperature where R_{xy}^{drag} drops to half its quantized value, that is, $h/2e^2$ (Fig. 1F, black line).

In Fig. 1G, we summarize the experimental phase diagram by plotting the temperature derivative of the counterflow resistance, dR_{xx}^{CF}/dT, versus d/l_B. Plotting this way emphasizes the three distinct regimes of the

magneto-exciton phase diagram: the low-temperature superfluidic condensate (phase I, $T < T_c$); the intermediate phase, where there is a dissipative channel (i.e., $R_{xx}^{CF} > 0$) but the two layers remain coupled through exciton formation (phase II, $T_c < T < T_{pair}$); and the high-temperature normal phase, where the layers are decoupled and most excitons are unbound (phase III, $T > T_{pair}$). We note that the temperature range over which dR_{xx}^{CF}/dT is finite-valued tracks reasonably well the T_c and T_{pair} phase boundaries identified from Fig. 1E and Fig. 1F, respectively; this indicates that R_{xx}^{CF} and R_{xy}^{drag} are correlated in this phase diagram and that dissipation continuously increases with temperature in phase II.

The experimental phase diagram shown in Fig. 1G additionally reveals distinct temperature behavior between the small d/l_B (strong coupling) and large d/l_B (weak coupling) regimes. At small d/l_B, T_{pair} is much larger than T_c, with a gradual evolution observed between the condensate phase (phase I) and the high-temperature layer-decoupled phase (phase III). This signifies that in the strong coupling limit, the exciton pairing establishes well above the condensation temperature, consistent with the behavior expected for a BEC condensate. By contrast, at large d/l_B, T_{pair} approaches T_c, reaching toward the BCS limit. The similarity of these behaviors at small and large d/l_B to the well-known temperature dependence of the BEC and BCS limits (Fig. 1A) establishes the graphene double layer as a uniquely tunable platform where fermion pair condensation can be studied in both strong- and weak-pairing regimes (*1*–*3*, *28*).

The condensate phase transitions of magneto-excitons in QHBs can be further examined in the

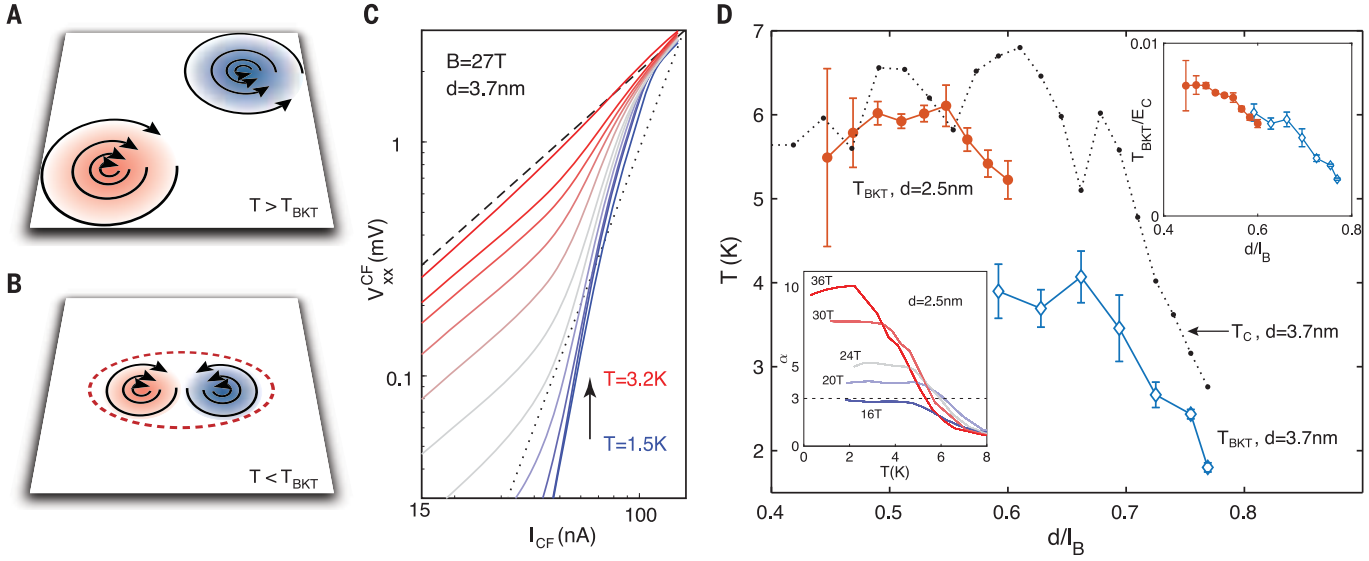

Fig. 2. BKT transition in the BCS regime. (**A** and **B**) Illustration of BKT transition. The circling black lines show the winding of the superfluid phase. Blue and red circles represent vortex and anti-vortex. When $T > T_{BKT}$, vortex and anti-vortex are free to move (A), whereas below the BKT temperature, they are bound into pairs (red dashed line) (B). (**C**) Counterflow current-voltage (*I-V*) relationship at $B = 27$ T in the $d = 3.7$ nm device at temperatures between $T = 1.5$ K and $T = 3.2$ K taken at approximately even temperature intervals. The dashed and dotted lines mark power-law exponents $\alpha = 1$ and 3, respectively. (**D**) BKT transition temperature as a function of d/l_B in two samples with interlayer separation of 3.7 nm and 2.5 nm (blue and red symbols, respectively). For comparison, the black dotted line shows T_c of the $d = 3.7$ nm sample from Fig. 1E. Bottom left inset: α extracted from the *I-V* curves as a function of temperature for select fields in the sample with $d = 2.5$ nm. Under high magnetic fields, α rises above 3 at low temperatures, as expected for a BKT transition. However, the value of α saturates at low temperatures; as the magnetic field drops, the saturation value decreases. Eventually, for smaller magnetic fields, T_{BKT} cannot be defined, as α saturates below 3 (see, e.g., the $B = 16$ T curve). Top right inset: BKT transition temperature after scaling to Coulomb energy E_c. Data from two samples with different interlayer separation collapse onto a universal line. The error bars in the plots are estimated from the uncertainty of α obtained from power-law fitting of the *I-V* curves.

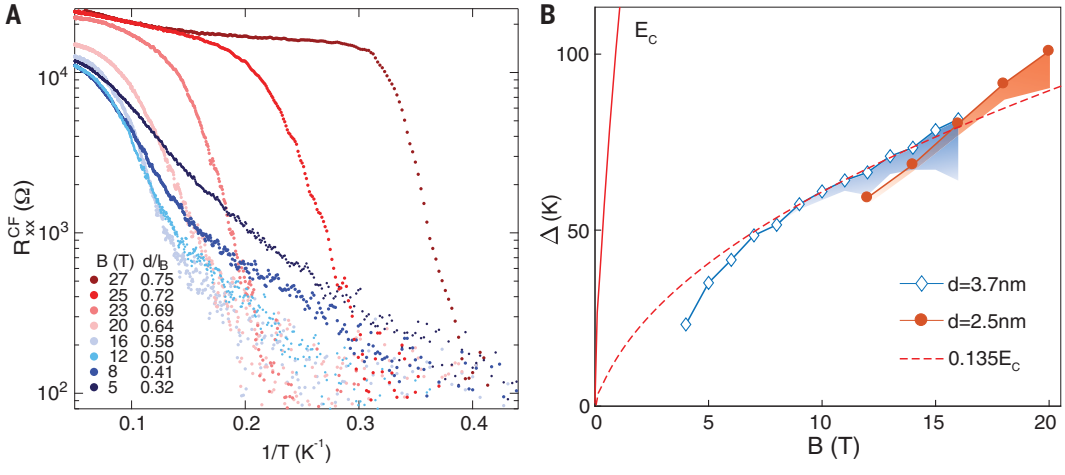

Fig. 3. Activation energy in the strong coupling regime. (**A**) Arrhenius plot of R_{xx}^{CF} measured at different magnetic fields in the $d = 3.7$ nm device. (**B**) Activation gap Δ as a function of magnetic field for two devices with different interlayer separation $d = 3.7$ nm and 2.5 nm. The red solid curve corresponds to the Coulomb energy, $E_c = e^2/\varepsilon l_B$, where e is the electron charge and ε is the dielectric constant of hBN. The red dashed curve shows $0.135E_c$.

context of two-dimensional (2D) phase transition nature. At $T < T_c$, the exciton condensate is expected to be a 2D superfluid described by the Berezinskii-Kosterlitz-Thouless (BKT) theory (*41*–*43*). To produce a counterflow voltage V_{xx}^{CF}, it is necessary that topological defects, namely vortices in the condensate order parameter (Fig. 2, A and B), should move across the sample in a direction perpendicular to the voltage gradient. Because the energy of an isolated vortex in a 2D superfluid diverges logarithmically with the size of the system, vortices can exist at low temperatures only in bound pairs of opposite signs (Fig. 2B). Counterflow resistance would not be produced by the motion of such pairs. As temperature rises, the vortices unbind at the critical temperature T_{BKT} (Fig. 2A). Above T_{BKT}, the movement of free vortices leads to a counterflow resistance. Below T_{BKT}, although the linear counterflow resistance is predicted to vanish, there can be a nonlinear response, giving a nonzero voltage at finite measuring currents. Specifically, it is predicted that for small counterflow currents I_{CF}, one should find a power-law relation: $V_{xx}^{CF} \propto (I_{CF})^{\alpha}$, where the exponent is given by $\alpha = 1 + [\pi\rho_s(T)/T]$, and $\rho_s(T)$ is the temperature-dependent phase-stiffness constant for the order parameter (*44*). According to BKT theory, $T_{BKT} = (\pi/2)\rho_s(T_{BKT})$, so α should be equal to 3 at T_{BKT} and should increase monotonically with decreasing temperature below T_{BKT} (*44*). In principle, the measured exponent should drop discontinuously to $\alpha = 1$ above T_{BKT}, but this decrease should be gradual for a finite measuring current.

Figure 2C plots experimental current-voltage (*I-V*) curves measured in the counterflow geometry in logarithmic scale. For our smallest measuring currents, below ~100 nA, we indeed observed power-law behavior, and we extracted a measured exponent $\alpha(T)$ by fitting the slope of the *I-V* curve at low currents. The result is plotted as a function of T in the bottom left inset of Fig. 2D. At large d/l_B, α increases with decreasing T, allowing us to extract T_{BKT} according to the criterion of $\alpha = 3$, for those α-T curves that go above $\alpha = 3$ at the lowest temperature. Figure 2D shows the experimentally obtained T_{BKT} over a large range of d/l_B for two graphene double-layer devices; in the large d/l_B limit, T_{BKT} obtained from the *I-V* curves follows the trend of the critical temperature T_c in Fig. 1G.

In the BCS framework, $\rho_s(T)$ collapses at the mean-field transition temperature T_m thanks to the proliferation of unpaired quasiparticles, and thus T_{BKT} is bounded by the mean-field transition temperature T_m (*44*). Because increasing d/l_B corresponds to weakening the interlayer BCS pairing, T_m (and thus T_{BKT}) should decline as d/l_B increases, in agreement with the experimental observation shown in Fig. 2D for $d/l_B > 0.5$. As d/l_B decreases from the BCS limit, we find that T_{BKT} first increases and then tends to saturate as the d/l_B reaches ~0.5, following the trend of T_c. Eventually the BKT transition becomes ill defined. Even for large magnetic fields, the measured value of α does not diverge as predicted for $T \to 0$, but instead saturates at a finite value (Fig. 2D, bottom left inset). The saturation value decreases with decreasing B, and eventually falls below 3. The mechanism behind the low-temperature saturation of α is unclear but may relate to the gradual evolution of counterflow resistance as a function of temperature at small d/l_B, including possible effects of disorder. Interestingly, we find that T_{BKT} measured from two samples collapses onto a universal curve after scaling with Coulomb energy, $E_c = e^2/\varepsilon l_B$ (Fig. 2D, top right inset). This shows the critical role of Coulomb interaction in the emergence of the exciton condensate in graphene double layers.

As B decreases, we move from the BCS limit (high B) to the BEC limit (low B) and find that the transition to the low-temperature condensation phase changes qualitatively. Figure 3A shows an Arrhenius plot of R_{xx}^{CF} versus temperature at fixed values of the applied magnetic field B. Whereas at large d/l_B a sharp jump in $R_{xx}^{CF}(T)$ occurs, consistent with the BKT transition described above, at small d/l_B the counterflow resistance exhibits a thermally activated behavior $R_{xx}^{CF}(T) \sim \exp(-\Delta/2T)$ with a well-defined Δ (Fig. 3A, blue traces).

Plotting Δ as a function of B in the small d/l_B regime provides insight into the relevant low-energy excitations in the BEC limit (Fig. 3B). For both samples, the plots are well fit by $\Delta = 0.135E_c$. Qualitatively, the trend of Δ with changing B field complies with the behavior of T_{pair} shown in Fig. 1A. In the BEC limit of the illustration (Fig. 1A), T_{pair}/E_F can be approximated to a zeroth-order constant; therefore, T_{pair} is proportional to E_F. In QHB, E_c plays the role of E_F, so it is not surprising that the energy scale of pairing scales with E_c. Quantitatively, we note that this value is an order of magnitude smaller than the energy to create a free electron and hole, indicating that the appearance of the finite resistance is not caused by unbinding of excitons. The most relevant collective excitations in the small d/l_B limit are predicted to be merons and anti-merons (*45*), which are charged topological vortices of the exciton condensate, with large core radii (*26*). Merons have core energies that are a fraction of E_c, and it can be argued that in the extreme limit of $d/l_B \to 0$, there may be a regime where the density of free merons leads to $R_{xx}^{CF} \sim \exp(-\Delta/2T)$, with Δ a fraction of E_c. Our estimation of Δ for the generation of a meron–anti-meron pair is ~$0.6E_c$ (*26*); because this value is much larger than the observed Δ, disorder might play a crucial role.

We note that similar activated behavior of the counterflow current has been observed in GaAs QHBs (*37*, *38*) in the regime of much larger d/l_B. The graphene QHB exhibits a sharp, nonactivated transition occurring in the BCS limit, where the counterflow resistance vanishes critically (fig. S2A) and the characteristic BKT type of *I-V* appears. These observations are absent in the GaAs QHBs. The cause of the distinct phenomenologies of the two systems remains uncertain, but we point out the following differences: The atomically thin interlayer separation of graphene QHBs allows us to access a much stronger coupling parameter range $d/l_B = 0.3$ to 0.8, as compared to $d/l_B = 1.3$ to 1.8 in GaAs (*36*–*38*, *46*). The small interlayer separation in graphene QHBs makes our system less susceptible to the influence of disorder and provides activation gaps that are two orders of magnitude larger than in GaAs.

Our results show that the adjustable pairing strength in graphene double-layer structures allows access to two distinct regimes of fermion pair condensation, characterized by strong and weak coupling strength, where we uncovered distinct transport behaviors and roles of topological excitations. This dynamical and continuous tunability of fermion pairing in a solid-state device opens the door to investigating the phenomenology of fermion condensates of various pairing strengths, and may lead to improved understanding of the connection between the BCS-BEC crossover and unconventional superconductivity.

REFERENCES AND NOTES

1. A. Leggett, S. Zhang, *The BEC-BCS Crossover: Some History and Some General Observations* (Springer, 2012).
2. M. Randeria, E. Taylor, *Annu. Rev. Condens. Matter Phys.* **5**, 209–232 (2014).
3. Q. Chen, J. Stajic, S. Tan, K. Levin, *Phys. Rep.* **412**, 1–88 (2005).
4. C. A. Sá de Melo, *Phys. Today* **61**, 45–51 (2008).
5. J. Bardeen, L. N. Cooper, J. R. Schrieffer, *Phys. Rev.* **108**, 1175–1204 (1957).
6. D. M. Eagles, *Phys. Rev.* **186**, 456–463 (1969).
7. A. J. Leggett, *J. Phys. Colloq.* **41**, C7-19 (1980).
8. P. Nozières, S. Schmitt-Rink, *J. Low Temp. Phys.* **59**, 195–211 (1985).
9. M. Randeria, J. M. Duan, L. Y. Shieh, *Phys. Rev. Lett.* **62**, 981–984 (1989).
10. T. Timusk, B. Statt, *Rep. Prog. Phys.* **62**, 61 (1999).
11. J. Tallon, J. Loram, *Physica C* **349**, 53–68 (2001).
12. Y. Cao *et al.*, *Nature* **556**, 43–50 (2018).
13. T. Bourdel *et al.*, *Phys. Rev. Lett.* **93**, 050401 (2004).
14. C. A. Regal, M. Greiner, D. S. Jin, *Phys. Rev. Lett.* **92**, 040403 (2004).
15. M. Bartenstein *et al.*, *Phys. Rev. Lett.* **92**, 203201 (2004).
16. M. W. Zwierlein *et al.*, *Phys. Rev. Lett.* **92**, 120403 (2004).
17. M. G. Ries *et al.*, *Phys. Rev. Lett.* **114**, 230401 (2015).
18. P. A. Murthy *et al.*, *Science* **359**, 452–455 (2018).
19. S. Rinott *et al.*, *Sci. Adv.* **3**, e1602372 (2017).
20. Y. Nakagawa *et al.*, *Science* **372**, 190–195 (2021).
21. L. Du *et al.*, *Nat. Commun.* **8**, 1971 (2017).
22. Z. Zhu *et al.*, *Sci. Rep.* **7**, 1733 (2017).
23. J. Eisenstein, *Annu. Rev. Condens. Matter Phys.* **5**, 159–181 (2014).
24. X. Liu, K. Watanabe, T. Taniguchi, B. I. Halperin, P. Kim, *Nat. Phys.* **13**, 746–750 (2017).
25. J. I. Li, T. Taniguchi, K. Watanabe, J. Hone, C. R. Dean, *Nat. Phys.* **13**, 751–755 (2017).

26. See supplementary materials.
27. B. I. Halperin, P. A. Lee, N. Read, *Phys. Rev. B* **47**, 7312–7343 (1993).
28. D. Jérome, T. M. Rice, W. Kohn, *Phys. Rev.* **158**, 462–475 (1967).
29. P. B. Littlewood *et al*., *J. Phys. Condens. Matter* **16**, S3597–S3620 (2004).
30. N. E. Bonesteel, I. A. McDonald, C. Nayak, *Phys. Rev. Lett.* **77**, 3009–3012 (1996).
31. G. Möller, S. H. Simon, E. H. Rezayi, *Phys. Rev. Lett.* **101**, 176803 (2008).
32. G. Möller, S. H. Simon, E. H. Rezayi, *Phys. Rev. B* **79**, 125106 (2009).
33. J. Alicea, O. I. Motrunich, G. Refael, M. P. A. Fisher, *Phys. Rev. Lett.* **103**, 256403 (2009).
34. I. Sodemann, I. Kimchi, C. Wang, T. Senthil, *Phys. Rev. B* **95**, 085135 (2017).
35. J. J. Su, A. H. MacDonald, *Nat. Phys.* **4**, 799–802 (2008).
36. M. Kellogg, I. B. Spielman, J. P. Eisenstein, L. N. Pfeiffer, K. W. West, *Phys. Rev. Lett.* **88**, 126804 (2002).
37. M. Kellogg, J. P. Eisenstein, L. N. Pfeiffer, K. W. West, *Phys. Rev. Lett.* **93**, 036801 (2004).
38. E. Tutuc, M. Shayegan, D. A. Huse, *Phys. Rev. Lett.* **93**, 036802 (2004).
39. X. Liu *et al*., *Phys. Rev. Lett.* **119**, 056802 (2017).
40. J. P. Eisenstein, A. H. Macdonald, *Nature* **432**, 691–694 (2004).
41. V. Berezinskii, *Sov. Phys. JETP* **34**, 610–616 (1972).
42. J. M. Kosterlitz, D. J. Thouless, *J. Phys. C* **6**, 1181–1203 (1973).
43. S. M. Girvin, *Boulder School 2000: Lecture Notes* (2000); https://boulderschool.yale.edu/2000/boulder-school-2000-lecture-notes.
44. B. I. Halperin, D. R. Nelson, *J. Low Temp. Phys.* **36**, 599–616 (1979).
45. S. M. Girvin, A. H. MacDonald, *Multicomponent Quantum Hall Systems: The Sum of Their Parts and More* (Wiley-VCH, 2007).
46. T. S. Lay *et al*., *Phys. Rev. B* **50**, 17725–17728 (1994).
47. X. Liu *et al*., Replication data for "Crossover between strongly coupled and weakly coupled exciton superfluids". Harvard Dataverse (2021); doi.org/10.7910/DVN/4TLQYI.

ACKNOWLEDGMENTS

We thank S. H. Simon, B. Lian, S. D. Sarma, I. Sodemann, I. Kimchi, M. Shayegan, and J. P. Eisenstein for helpful discussion. **Funding:** Supported by the US Department of Energy (DOE), Office of Science, Basic Energy Sciences, under award DE-SC0019481 (C.R.D.); DOE award DE-SC0012260 for device fabrication and measurement (X.L.); DoD Vannevar Bush Faculty Fellowship N00014-18-1-2877 (P.K.); and the Elemental Strategy Initiative conducted by the MEXT, Japan, A3 Foresight by JSPS and the CREST (JPMJCR15F3), JST (K.W. and T.T.). Sample preparation at Harvard was supported by ARO MURI (W911NF-14-1-0247). Sample fabrication at Columbia University was supported by the Center for Precision-Assembled Quantum Materials (PAQM), a Materials Science and Engineering Research Center (MRSEC) through NSF grant DMR-2011738. The theoretical analysis was supported in part by the Science and Technology Center for Integrated Quantum Materials, NSF grant DMR-1231319. A portion of this work was performed at the National High Magnetic Field Laboratory, which is supported by NSF Cooperative Agreement DMR-1644779 and the state of Florida. Nanofabrication at the Center for Nanoscale Systems at Harvard was supported by NSF NNIN award ECS-00335765. **Author contributions:** X.L., J.I.A.L., J.H., P.K., and C.R.D. conceived the experiment. X.L. and J.I.A.L. fabricated the samples, performed the measurements, and analyzed the data. B.I.H. conducted the theoretical analysis. K.W. and T.T. supplied hBN crystals. X.L., J.I.A.L., P.K., B.I.H., and C.R.D. wrote the paper with input from all other authors. **Competing interests:** The authors declare no competing interests. **Data and materials availability:** The data from this study are available at the Harvard Dataverse (*47*).

SUPPLEMENTARY MATERIALS

10 December 2020; accepted 16 November 2021
10.1126/science.abg1110

Crossover between strongly coupled and weakly coupled exciton superfluids

Xiaomeng Liu, J. I. A. Li, Kenji Watanabe, Takashi Taniguchi, James Hone, Bertrand I. Halperin, Philip Kim, and Cory R. Dean

Science, **375** (6577), .
DOI: 10.1126/science.abg1110

Following a crossover

Superfluidity in fermionic systems occurs through the pairing of fermions into bosons, which can undergo condensation. Depending on the strength of the interactions between fermions, the pairs range from large and overlapping to tightly bound. The crossover between these two limits has been explored in ultracold Fermi gases. Liu *et al*. observed the crossover in an electronic system consisting of two layers of graphene separated by an insulating barrier and placed in a magnetic field. In this two-dimensional system, the pairs were excitons formed from an electron in one layer and a hole in the other. The researchers used magnetic field and layer separation to tune the interactions and detected the signatures of superfluidity through transport measurements. —JS